ACS NANO

www.acsnano.org

ARTICLE

Downloaded via LIB4RI on April 12, 2022 at 12:22:47 (UTC).
See https://pubs.acs.org/sharingguidelines for options on how to legitimately share published articles.

Engineering Optically Active Defects in Hexagonal Boron Nitride Using Focused Ion Beam and Water

Evgenii Glushkov,*,# Michal Macha,# Esther Räth, Vytautas Navikas, Nathan Ronceray, Cheol Yeon Cheon, Aqeel Ahmed, Ahmet Avsar, Kenji Watanabe, Takashi Taniguchi, Ivan Shorubalko, Andras Kis, Georg Fantner, and Aleksandra Radenovic*

Cite This: *ACS Nano* 2022, 16, 3695−3703

Read Online

ACCESS | Metrics & More | Article Recommendations | Supporting Information

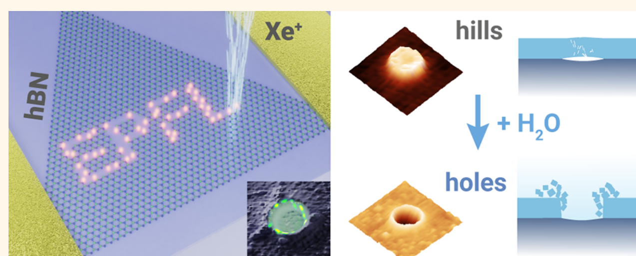

ABSTRACT: **Hexagonal boron nitride (hBN) has emerged as a promising material platform for nanophotonics and quantum sensing, hosting optically active defects with exceptional properties such as high brightness and large spectral tuning. However, precise control over deterministic spatial positioning of emitters in hBN remained elusive for a long time, limiting their proper correlative characterization and applications in hybrid devices. Recently, focused ion beam (FIB) systems proved to be useful to engineer several types of spatially defined emitters with various structural and photophysical properties. Here we systematically explore the physical processes leading to the creation of optically active defects in hBN using FIB and find that beam−substrate interaction plays a key role in the formation of defects. These findings are confirmed using transmission electron microscopy, which reveals local mechanical deterioration of the hBN layers and local amorphization of ion beam irradiated hBN. Additionally, we show that, upon exposure to water, amorphized hBN undergoes a structural and optical transition between two defect types with distinctive emission properties. Moreover, using super-resolution optical microscopy combined with atomic force microscopy, we pinpoint the exact location of emitters within the defect sites, confirming the role of defected edges as primary sources of fluorescent emission. This lays the foundation for FIB-assisted engineering of optically active defects in hBN with high spatial and spectral control for applications ranging from integrated photonics, to nanoscale sensing, and to nanofluidics.**

KEYWORDS: *hexagonal boron nitride, hBN, vdW materials, quantum emitters, optically active defects, defect engineering, focused ion beam*

INTRODUCTION

Optically active defects in van der Waals (vdW) materials have attracted a lot of attention recently, finding applications in the fields of nanophotonics and nanofluidics.[1−5] In particular, hexagonal boron nitride (hBN) has emerged as a promising material platform, hosting a plethora of optically addressable defects within its large bandgap (≈6 eV).[6] Initially established as bright and stable single-photon sources,[7] defects in hBN have since been proven to be useful for the integration into hybrid photonic devices,[8] super-resolution imaging,[9−14] and studying complex charge dynamics in aqueous environments.[15,16] Moreover, several recent works have demonstrated spin-dependent emission from defects in hBN[17] at room temperature,[18−20] opening numerous applications for this material platform.[21]

Defects in hBN are either randomly formed during growth,[10,22] postgrowth doping,[23] or exfoliation from bulk crystals[24,25] or can be intentionally induced in the pristine/unirradiated material using large-area irradiation with ions[11,26,27] or neutrons[28] or using high-temperature annealing.[7] While these approaches reliably produce quantum emitters in hBN, they result in randomly spatially distributed defects, thus complicating their proper and reliable characterization using correlated microscopy[29] and hindering their applications in

Received: August 16, 2021
Accepted: February 22, 2022
Published: March 7, 2022

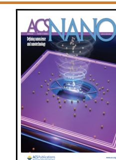

© 2022 The Authors. Published by American Chemical Society

https://doi.org/10.1021/acsnano.1c07086
ACS Nano 2022, 16, 3695−3703

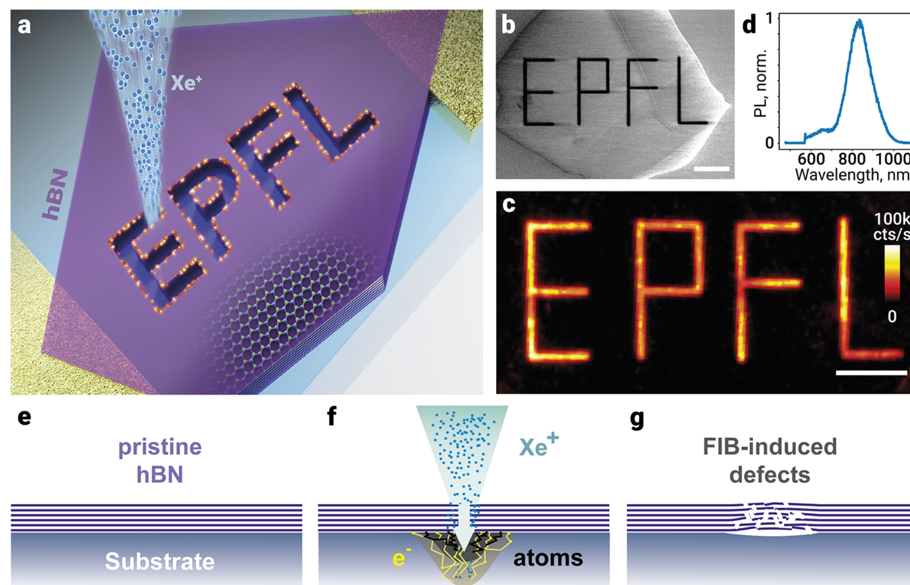

Figure 1. Generation of FIB-induced optically active defects in exfoliated hBN flakes. (a) Schematic representation of the defect writing process on a pristine/unirradiated hBN flake using Xe FIB. Gold electrodes on the sides reduce charging effects during irradiation. (b) Scanning electron microscope (SEM) image of a patterned flake inside the FIB chamber. (c) Fluorescence image of the generated pattern of optically active defects from a confocal microscope. Imaging was done in water. (d) Characteristic spectrum of FIB-induced defects, taken from a dried sample in air. The sharp little peak, seen on the short-wave side, is the Raman peak of the hBN material. (e−g) Simplified schematic of the FIB-induced defect generation process, a result of Xe ions interacting with the substrate, which is partially milled (f), creating a defected region and a void beneath the hBN flake (g). Scale bars: 10 μm (a, inset) and 5 μm (e).

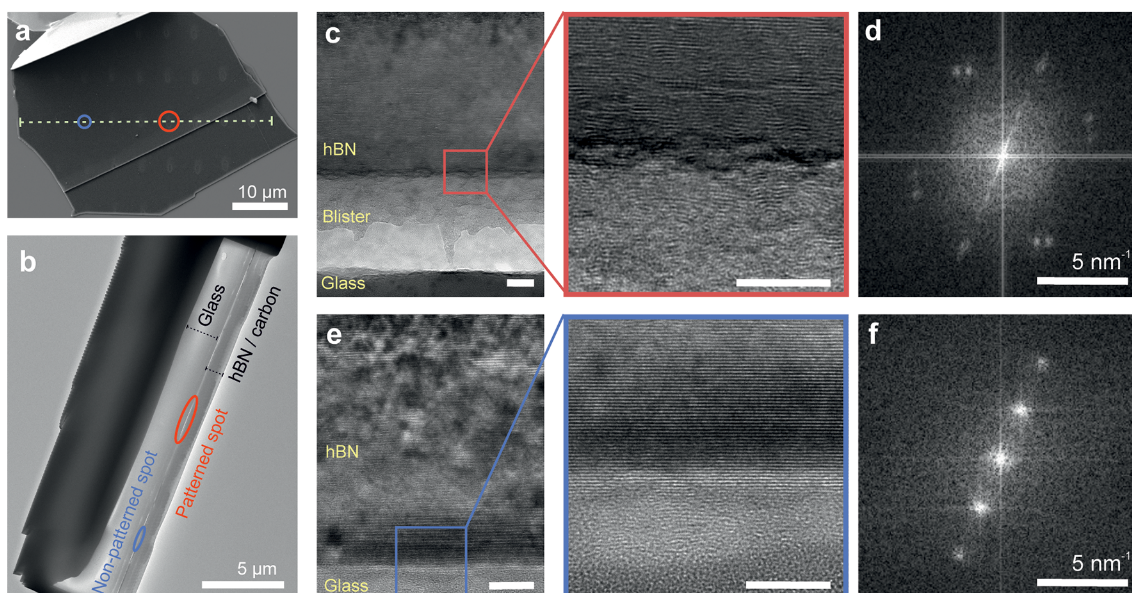

Figure 2. Exploring mechanical effects of FIB irradiation using TEM. (a) Irradiated hBN flake on a glass substrate, with 3 μm-spaced defect sites (seen as brighter spots on top of a dark hBN surface, marked with the dotted line). (b) Lamella of the hBN flake cross-section cut along the dashed line marked in (a). A thin layer of carbon was sputtered on top of the flake to prevent charge accumulation. (c) Cross-sectional image of the irradiated hBN area and (d) corresponding fast Fourier transform (FFT) compared to (e) the pristine/unirradiated area image of the hBN/glass interface and its FFT (f) shows an evident mechanical deterioration of hBN layers and the local amorphization of the material. Scale bars: 10 nm.

integrated devices for nanophotonics[8] and nanofluidics (*e.g.*, to systematically study the dynamics of charge transfer at liquid−solid interfaces[15,16]). Recent attempts to generate defects in hBN at precise spatial locations included strain engineering through either transfer/exfoliation[30] of hBN flakes or growth of hBN films on patterned substrates,[31] offering scalability, but limited subsequent integration. Other patterning approaches included the use of pulsed lasers[32,33] and focused electron[34] and ion beams[19,35] to locally damage the hBN lattice and generate emitters with desired properties.

Focused ion beam (FIB) seems an especially appealing technique for the generation of optically active defects in vdW materials due to its versatility, high resolution, ease of use, and scalability. Notably, FIB has found widespread use for

https://doi.org/10.1021/acsnano.1c07086
ACS Nano 2022, 16, 3695−3703

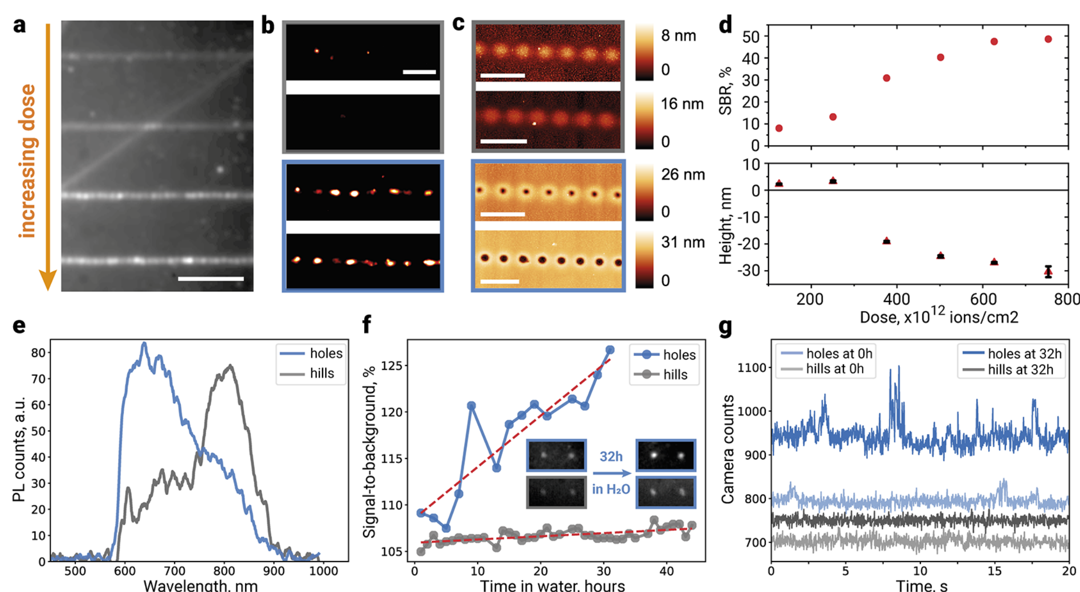

Figure 3. Optical and morphological characterization of irradiated defect sites. (a) Wide-field fluorescence image of an hBN flake with FIB-irradiated horizontal line patterns of a gradually increasing dose, which results in the creation of optically active defects of increasing intensity. For all measurements in this figure 561 nm laser excitation is used. Imaging is performed in DI water, pH 5.8. (b) Zoom-ins from (a), processed using a localization microscopy algorithm,[42] reveal two different types of emission: dim diffused emitters (type I), which are not localized by the algorithm due to low signal-to-noise ratio (SNR), and bright localized ones (type II), which are clearly visible. (c) AFM scans of respective areas. Two types of emitters from optical images can be easily correlated with the difference in morphology, depending on the irradiation dose: hills are formed for lower doses and holes for higher ones. Imaging was done in air, after thoroughly drying the immersed sample with a nitrogen gun. (d) Extracted signal intensities (signal-to-background ratio, SBR) and height/depth of the FIB-induced defects *vs* irradiation dose, showing the dose-dependent hill-to-hole transition. (e) Spectra of two defect types, acquired in water. When measuring in air, only the peak around 800 nm is distinguishable (Figure 1d). (f) Change in the brightness of two types of emitters after a long immersion in water. (g) Comparison of the temporal dynamics of hill *vs* hole emitters before and after the long immersion. Scale bars: 5 μm (a) and 1 μm (b, c).

patterning of 2D materials as a resist-free method,[36,37] mitigating omnipresent polymer contamination of the patterned material. And the emergence of commercially available plasma FIB (PFIB) machines, employing ions of inert gases, such as argon and xenon, instead of liquid metals, has solved the long-standing problem of sample contamination by gallium ions in traditional FIB systems.[38,39] Nevertheless, while deterministic defect generation in hBN using FIB has been recently demonstrated,[19,35] achieving submicron spatial accuracy, a clear understanding of the FIB irradiation effects and the formation of defect sites in hBN is lacking.

In this work, we present a systematic study of these effects, arising from the beam interacting not only with the thin layer of hBN itself, but also with the underlying substrate, performing transmission electron microscopy (TEM) analysis of cross-sections of irradiated hBN flakes. We further show that the FIB-induced defects are strongly influenced by the environment in which the irradiated samples are placed. In particular, we uncover a mechanism of water-assisted etching of FIB-irradiated hBN defects, leading to drastic structural and optical transitions in irradiated sites. Moreover, by utilizing a state-of-the-art super-resolution microscopy technique correlated with atomic force microscopy (AFM) imaging, we explicitly show the localization of emitters in hBN at the rim of FIB-induced defect sites, in good agreement with a literature hypothesis.[35]

RESULTS AND DISCUSSION

We employed the Helios G4 Xe PFIB system to investigate the influence of Xe ion irradiation on pristine hBN flakes, containing very few intrinsic defects.[40] The flakes were prepared on cleaned SiO_2 substrates with gold markers and grounding electrodes by mechanical exfoliation from high-quality hBN crystals,[41] resulting in a typical thickness of hBN flakes of 10−100 nm. Directly after exfoliation, the samples were loaded into the Xe FIB and irradiated with a predefined pattern (Figure 1a). The irradiated flakes were briefly checked in the built-in SEM, clearly demonstrating the FIB-induced changes in the morphology of the sample (Figure 1b). After unloading from the FIB chamber, the samples were inspected on a home-built fluorescence microscope, confirming the creation of optically active defects at the irradiated sites on hBN flakes (Figure 1c). The spectral characteristics of FIB-patterned defects qualitatively matched the previously reported ones for Xe FIB,[19] with the broad emission peak centered around 830 nm, shown in Figure 1d (see Methods for details). The simplified mechanistic understanding of these changes is shown in Figure 1e−g, where defects are generated as a result of Xe ions interacting with the substrate, creating showers of backscattered electrons and sputtered ions that locally damage the crystalline structure of hBN layers.

To verify the structural changes induced on hBN flakes by the ion beam, a detailed high-resolution transmission electron microscopy (TEM) study of the milled area cross-section was performed (Figure 2). An hBN flake irradiated with typical experimental parameters (see Methods) was cut along the irradiated spots (Figure 2a) with a Ga FIB system to create a thin lamella (Figure 2b) suitable for TEM imaging. A high-resolution TEM image of the hBN/glass area on the irradiated spot (Figure 2c) shows visible signs of mechanical damage and

https://doi.org/10.1021/acsnano.1c07086
ACS Nano 2022, 16, 3695−3703

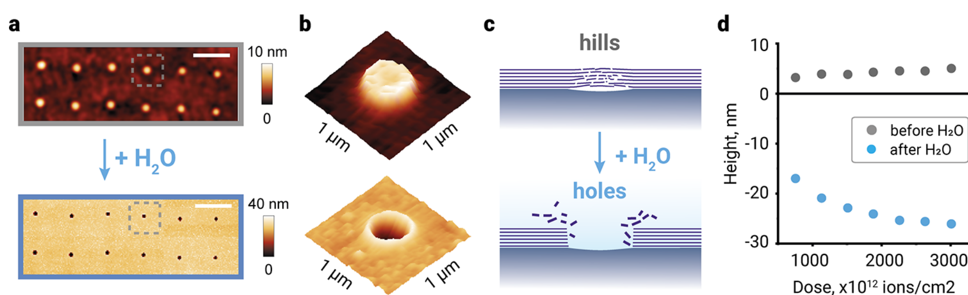

Figure 4. Water-assisted etching of irradiated defect sites. (a) AFM images of the same area on the irradiated hBN flake before and after immersion in water. Scale bar: 3 μm. (b) Pseudo-3D reconstruction of a single defect site before (top) and after water (bottom). (c) Schematic representation of the water-assisted hill-to-hole transition. (d) Dependence of the average peak height/depth of irradiated sites on irradiation dose (before and after water).

perforation caused by the PFIB on the hBN flake layers. Most of the damage is seen at the hBN/glass boundary due to the ion collision cascades, secondary electron emission, and substrate particle sputtering occurring in the interaction volume area underneath the patterned spot (schematically marked in Figure 1c). These effects lead to the hBN milling selectively occurring from beneath the flake, at the hBN/glass interface. Consecutively, this leads to the creation of the blister in between the hBN and glass substrate filled with the milled debris comprising amorphized and recrystallized hBN as well as particles sputtered from within the substrate. The fast Fourier transform (FFT) of the irradiated flake area (Figure 2d) shows signs of substantial amorphization and mechanical damage (smearing of the FFT pattern) of the hBN crystal lattice, which can be associated with hBN blistering. The PFIB milling damage is especially visible when compared to the unirradiated, pristine hBN/glass interface area (Figure 2e) and its corresponding, clear FFT (Figure 2f) image. Further details of the TEM-based study of irradiated sites are given in Figure S1.

To explore the optical properties of FIB-induced defects, we have used both a home-built confocal setup and a wide-field super-resolution microscope, optimized for single-molecule localization microscopy (SMLM).[11] We started with an hBN flake irradiated with line patterns of varied irradiation dose (1–8 × 10^{14} ions/cm^2, Table S1) to see how it affects fluorescent emission from defects. From the averaged image stack, shown in Figure 3a, one can see four horizontal lines of varying intensity corresponding to the irradiated pattern of a gradually increasing dose. The zoom-ins of each of these lines in Figure 3b are processed using an SMLM algorithm[42] to precisely localize the isolated emission spots. However, one can see that in the top two the localization algorithm fails to localize the emitters, as their emission intensity is rather dim and diffused, resulting in low signal-to-noise ratio (SNR) and low signal-to-background ratio (SBR) values of ∼5–10%. In contrast to that, the emitters in the bottom two lines are easily localized and are seen as regular bright spots with an SBR of ∼30–50% and ∼500 nm pitch distance (Figure S2).

To understand the origin of this emission difference, we performed AFM measurements on the same lines (Figure 3c). One can immediately see that two types of emitters correspond to either hill-type or hole-type structures created by the FIB depending on the irradiation dose. This dose-dependent transition of irradiated hBN areas is shown in Figure 3d and in more detail in the Supporting Information (Figure S2). Focusing on the optical properties of the optically active defects hosted within created hills and holes, we show that their differences go much beyond just emission intensity. In Figure 3e one can see the appearance of another spectral emission peak around 650 nm, measured from hole defects in water, while hill defects still show predominant emission around 800 nm. While the microscopic origin of this spectral transition is not clear, one can attribute it to the dangling bonds[43] appearing at the edge of the created holes in hBN. The 800 nm emission is also present in the spectrum of holes and is attributed to the remaining damaged material and/or strain around the hole. These observations suggest a possible conversion from intrinsic defects in hBN, likely, boron vacancies,[18,19] to extrinsic ones, influenced by the liquid environment. We further discuss the transitions between the two defect types and their corresponding emission lines, depending on the irradiation dose, as well as their spatial distribution in Figures S6–S8.

Another difference between the two defect types concerns the long-term evolution of the measured emission from holes *vs* hills when the sample is immersed in an aqueous solution for a long time (tens of hours). In Figure 3f one can see the steady increase in the signal intensity for holes and an absence of such increase for hills. This graph was obtained by analyzing the time-lapse images of the irradiated area, fitting the maximal intensity value at each defect site and normalizing it to its local background. An example of such images before and after the time lapse is shown in the inset, and the full protocol can be found in Figure S3. Both the origin of this increase of fluorescence intensity and its behavior at longer time intervals are yet to be studied (Figure S4). Finally, the temporal traces from both types of defects in the steady state, shown in Figure 3g, demonstrate sharp transitions between different intensity levels (blinking) for the emission originating from holes, but not from hills. This blinking behavior is further intensified after an extended stay in water, which we link to the accumulation of dangling bonds and functional groups in the circumference of hole structures and enhanced interaction with diffusing charges.[15] The exact chemical composition of the defect sites is not yet known and remains the topic of future studies.

Additional characterization of the optical properties of the created hill- and hole-type defects is shown in the Supporting Information. Figure S5 shows the recorded bleaching, lifetime, and saturation curves, while Figures S6–S11 focus on the spectral properties of defects. The observed optically detected magnetic resonance (ODMR) at 3.4 GHz (Figure S 5d) deserves special attention, closely matching the previously reported one[19] and verifying the creation of spin defects in the hBN lattice using FIB. Based on our observations and results from the literature,[18,19,21] one can conclude that the spin-

https://doi.org/10.1021/acsnano.1c07086
ACS Nano 2022, 16, 3695–3703

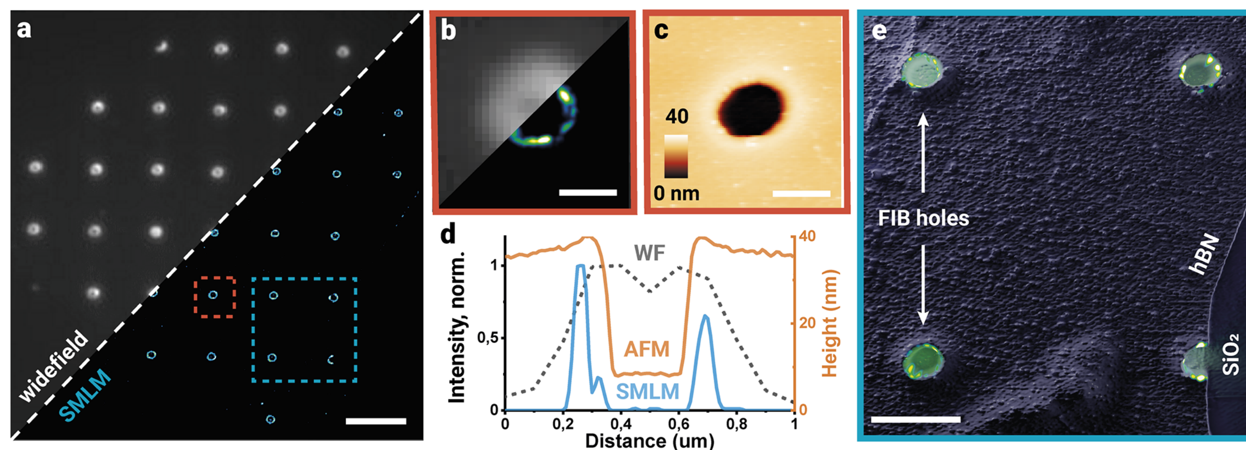

Figure 5. Correlated super-resolution and atomic force microscopy of FIB-induced defects in hBN. (a) Averaged fluorescence image of an irradiated hBN flake (2D array of isolated defects, 3 μm apart), overlaid by the super-resolved image of the same flake. (b) Zoom-in of the dashed red area around the isolated defect site (overlaid wide-field/SMLM). (c) AFM scan of the same area, perfectly matching fluorescence data. (d) Line profiles from zoom-ins in (b) and (c), showing cross-sections of the same defect site in wide-field, SMLM, and AFM images. (e) Correlated AFM-SMLM image of four defect sites from a dashed blue area in (a), clearly showing precise spatial localization of optically active emitters at the rim of the holes, formed by FIB irradiation and activated by water. Scale bars: 3 μm (a), 400 nm (b, c), and 1 μm (e).

dependent emission comes primarily from the 830 nm peak, for both hole and hill defects. However, further studies are needed to clarify this question and to uncover the reason that the ODMR at sub-GHz frequencies, reported for the 600 nm emission line,[17,20] could not be observed for the created hole-type defects.

Following the structural−optical transitions between two types of FIB-induced defects, immersed in the imaging medium (DI water), we explored in more detail its influence on the formation of defects. Having obtained an AFM scan of a marked area of an hBN flake just after FIB irradiation, we observed the creation of only hill-type structures, even though the irradiation doses were high enough to create holes (in comparison to Figure 3). However, after immersing the sample in water and imaging the same area with AFM again we have noticed the immediate creation of holes in the irradiated regions (Figure 4a). The observed hill-to-hole transition happened at a time scale of 2 consecutive AFM scans of the same area (∼20 min long), suggesting a fast dissolution process (Figure S12) in comparison to the slow SBR increase of the fluorescent signal in Figure 3f. The 3D zoom-ins of the selected defect before and after immersion in water are shown in Figure 4b and perfectly illustrate the water-mediated hill-to-hole transition. Figure 4c shows a simplified schematic of the etching process, where the damaged hBN material at the irradiated sites (seen in Figure 2) is quickly removed by water. However, once the holes are created, their lateral size and depth do not noticeably change both in air and in water over the course of days (Figure S13). This indicates that only damaged hBN material is removed by water.[44]

The dependence of the created height/depth of the hills/holes, respectively, on the irradiation dose is shown in Figure 4d, suggesting a continuous hill-to-hole transition at a lower dose (∼3×10^{14} ions/cm^2 on Figure 3d). The slight linear increase in the height of the hills at longer irradiation times probably comes from either more sputtering or a continuous cavity growth underneath hBN, which makes the thin flake bulk up. The saturation behavior for the depth of the created hills can be explained by water fully etching through the hBN flake and reaching the substrate material. Combining these findings with data from Figure 3, we conclude that the observed hill-to-hole transition is caused by water and is dose-dependent, *i.e.*, starting from a certain FIB irradiation dose, which mechanically damages the hBN material enough for the water to dissolve it. This claim is supported by the TEM inspection of the irradiated areas in Figure 2 and literature studying the reactivity of mechanically damaged bulk hBN in water.[44] This defect formation process is specific for hBN flakes deposited on substrates with thicknesses much larger than the typical beam penetration depth (<100 nm),[19] due to the FIB−substrate interaction effects, illustrated in Figure 1e−g and confirmed using TEM in Figure 2. No hole formation or subsequent structural or optical changes in water were observed for FIB-irradiated hBN flakes which were suspended over holes or supported on thin membranes. An example of such a sample and its AFM analysis directly after irradiation is shown in Figure S15, demonstrating the creation of hole defects created by the ion beam in the suspended hBN without any influence of water.

Finally, to better understand the origins of the emission, we performed correlative SMLM and AFM imaging of the hole defects. Briefly, we first acquired stacks of thousands of wide-field images of irradiated hBN flakes with isolated defect sites immersed in DI water. The averaged image from one of these stacks is shown in the top-left part of Figure 5a, while in the bottom-right part we show a reconstructed super-resolved image, processed by a state-of-the-art localization algorithm.[45] In some of the bright defect sites in the averaged wide-field image one can notice the presence of a darker central region, hinting on the probable emission from the edges of the formed hole, as was suggested in the literature.[35] Super-resolved images of FIB-induced defects provide the direct evidence of such edge-related emission, which is shown in detail in the zoom-in in Figure 5b. The acquired AFM image of the same area matches well the SMLM data (Figure 5c). To further verify and visualize the spatial distribution of emitters, we show the overlaid image in Figure 5d, where one can clearly see the emergence of fluorescent emission from the edge of the hole defects.

https://doi.org/10.1021/acsnano.1c07086
ACS Nano 2022, 16, 3695−3703

While the hole defects, demonstrated in Figure 5, are relatively large, smaller sub-100 nm defects were successfully created using the current technique and measured with AFM (see Figure 4a and Figure S14). However, having dense emitters on the rim of the defect sites hinders their analysis with SMLM-based super-resolution optical microscopy. Further optimization of irradiation parameters and imaging conditions will enable the use of the FIB-created emitters for multiple super-resolution microscopy modalities. Moreover, better spatial resolution and a smaller waist of the ion beam, such as in the helium ion microscopes (HIMs), can further decrease the affected defect sites by 1−2 orders of magnitude,[46−48] enabling deterministic creation of atomically small isolated defects with nanometer precision emitting single photons. Further miniaturization of optically active defects to below 100 nm scale should also facilitate in-depth studies of nanofluidic phenomena at the liquid−solid interfaces[15,16] with precise spatial control over the nanoscale charge dynamics (*e.g.*, proton hopping/diffusion). Finally, such spatially engineered fluorescent defects, created using a polymer-free method, can enable nanoscale sensing of liquids in a confined environment (*e.g.*, nanoslits[3−5]), as well as charges in heterostructures.[49]

CONCLUSION

We presented a systematic study of the focused ion beam interactions with supported thin exfoliated hexagonal boron nitride flakes, leading to the creation of optically active spin defects. We showed that the defect creation is the result of the ion beam interacting not only with the thin hBN flakes but also with the substrate, on which it is supported. Moreover, both the structural and optical properties of the induced defects are dose-dependent and undergo irreversible transitions in aqueous solutions, representing a particular mechanism of water-assisted formation of FIB-irradiated hBN defects. By utilizing super-resolution microscopy correlated with AFM imaging, we were able to explicitly show the localization of emitters at the rim of the created defect site. Our findings lay the foundation for FIB-assisted engineering of optically active defects in hBN with high spatial control for nanophotonics, nanoscale sensing, and nanofluidics.

METHODS

Sample Preparation. hBN flakes from high-quality crystals[41] were exfoliated onto glass coverslips (no. 1.5 micro coverglass, Electron Microscopy Sciences, 25 mm in diameter), prepatterned with gold markers for easier navigation and electrode mesh to prevent accumulation of charges. Exfoliation was done using either tape or gel-pack stamps. The flakes for TEM grids (Norcada, NT025C) were polymer-transferred. Si/SiO_2 substrates have also been used, with similar patterning results.

FIB Irradiation. Irradiation and hBN patterning were done on Helios G4 PFIB UXe system with a Xenon Plasma FIB column. All experiments were done at 30 kV with a 100 pA Xe beam with varying parameters of dwell time and pitch distance between irradiated spots. By varying the dwell time from 100 μs to up to 2 ms we effectively increase the irradiation dose and pattern outcome in the form of irradiated spot size. Pitch distance is typically set to 3 μm for studying isolated defects and between 300 and 500 nm in case of tighter arrays and line patterns. Typical ion fluence/dose ranges from 1.2×10^{14} to 2.5×10^{15} ions/cm^2 for a dwell time range of 100 μs to 2 ms. Several tens of samples have been routinely created using this technique.

Optical Inspection. Wide-field imaging has been done on a custom wide-field fluorescence microscope, described elsewhere.[10,11] Briefly, the emitters are excited using either a 488 or 561 nm laser (monolitic laser combiner 400B, Agilent Technologies), which is collimated and focused on the back focal plane of a high-numerical aperture oil-immersion microscope objective (Olympus TIRFM 100×, NA 1.45). This creates a wide-field illumination of the sample in an area of ∼25 μm^2.

Fluorescence emission from the sample is collected by the same objective and spectrally separated from the excitation light using dichroic and emission filters (ZT488/561rpc-UF1 and ZET488/561m, Chroma) before being projected on an EMCCD camera (Andor iXon Life 897) with an EM gain of 150. An additional spectral path, mounted in parallel to the localization path, allows for simultaneous measurements of the emission spectra from individual emitters.[11] The sample itself is mounted in a sealed fluidic chamber, which is placed on a piezoelectric scanner (Nano-Drive, MadCity-Labs) for fine focus and drift compensation using an IR-based feedback loop, which is especially important for long-term measurements. The typical exposure time is 20−50 ms and the typical laser power is 50−100 mW for the wide-field excitation area of 2×10^3 μm^2, resulting in a power density of 2.5−5 kW/cm^2. A typical acquired image stack contained 2000−10 000 frames.

Confocal imaging was done on two different setups, utilizing either 532 or 561 nm excitation lasers and APDs as well as spectrometers to detect the emitted light. The first setup was used to obtain both emission and absorption spectra of defects to make their 2D spectral maps. However, due to the limitations in construction, this setup could only be used to image samples in air. In order to perform emission measurements, a diode-pumped solid state (DPSS) laser (DJ532-40, ThorLabs) at 532 nm was used. The laser beam was passed through a single-mode fiber (P3-460B-FC-1, ThorLabs) to obtain a Gaussian beam profile. Afterward, a narrow bandpass filter (FL05532-1, ThorLabs) was placed in the beam path to remove any unwanted features from the laser spectrum. A 100×, 0.9 NA objective (MPLFLN, Olympus) focused the beam on the sample and collected the emission. The sample was mounted vertically on a piezoelectric stage (Nano-Drive, MadCityLabs), and a raster scan was performed to obtain the spectral maps. The laser line was removed from the emission spectra by a long-pass filter (FELH0550, ThorLabs), and the signal was recorded using a spectrograph (Kymera 193i, Andor) with a CCD (iDus, Andor). For absorption measurement, the sample was illuminated from the back by a calibrated halogen lamp (SLS201L, ThorLabs). The transmitted light was collected, on the opposite side of the sample, by a 100×, 0.9 NA objective (MPLFLN, Olympus), and the spectrum was recorded with the CCD. In order to extract the absorption, a measurement was first made on the substrate and used a background signal.

To compensate for this, we utilized a second confocal setup in an inverted microscope configuration, allowing us to image samples in liquid. Here the emission was split between two fiber-coupled APDs (SPCM-AQRH, Excelitas) in an HBT configuration. One of the APDs could be switched with a fiber-coupled spectrometer (QE Pro, Ocean Optics) to measure the emission spectra in liquid. The setup could also perform lifetime and photon correlation measurements using the PicoHarp TCSPC module (PicoQuant).

TEM Imaging. The lamella for cross-section imaging was cut using the Zeiss NVision 40 CrossBeam system. The irradiated flake chosen for cross-section imaging was patterned using default array parameters, *i.e.*, 30 kV, 100pA Xe FIB. High-resolution TEM imaging was performed at the Talos L120C G2 using an 80 kV electron beam.

AFM Imaging and Image Processing. For the AFM imaging a customized AFM, consisting of a Dimension Icon AFM head (Bruker) mounted above an optical microscope (Olympus IX83), was used.[50] The position of the hBN flakes with respect to the cantilever was detected with the optical microscope. AFM images in air were recorded at a line rate of 0.5 Hz with RTESPA-150 cantilevers (Bruker) with a nominal spring constant of 6 N m^{-1} in tapping mode. The cantilever drive frequency and amplitude were determined by automated cantilever tuning. AFM images in fluid were acquired at 0.5 Hz line rate using ScanAsyst Fluid cantilevers (Bruker) with a nominal spring constant of 0.7 N m^{-1} in PeakForce quantitative nanomechanical mode at an oscillation rate of 1 kHz

https://doi.org/10.1021/acsnano.1c07086
ACS Nano 2022, 16, 3695−3703

and a force set point of 3 nN. The images were processed with standard scanning probe software (Gwyddion).

SMLM Processing. Acquired image stacks from the wide-field microscope were processed using several SMLM algorithms: ThunderSTORM,[42] SOFI, and DECODE,[45] a recent deep-learning-based localization algorithm. DECODE processing can be beneficial in this case, as the emitter density around the rim is high (Figure S16). Standard SMLM algorithms such as Thunderstorm[42] require localization filtering based on fitted point-spread function size and a lengthy multiemitter fitting procedure to perform equally well (Figures S16–S18). To utilize DECODE, we trained the neural network provided by the authors using simulated frames with a high density of emitters ($5\ \mu m^{-2}$), a realistic intensity distribution (1000 ± 800 photons/event), and the experimental point spread function calibrated with fluorescent beads.

Another approach to analyze such type of data with dense emitters is to use the super-resolution optical fluctuation imaging (SOFI), which better tolerates the high density of emitters, and similarly DECODE shows the clear existence of the fluorescent rim at the edge of hole defects (Figure S17). SOFI images were processed using a previously published algorithm.[51] Both SOFI and DECODE approaches have allowed to clearly resolve rims of the defect sites, but DECODE led to fewer image artifacts than SOFI.

ASSOCIATED CONTENT

Supporting Information

The Supporting Information is available free of charge at https://pubs.acs.org/doi/10.1021/acsnano.1c07086.

> TEM micrographs of FIB-cut hBN lamella, analysis of FIB-induced line patterns of structural and optically active defects, calculating signal-to-background ratio values from processed wide-field images, SBR evolution in time, additional characterization of optical properties of FIB-induced defects, spectral dependence of fluorescence from induced defects on irradiation dose, emission peak ratio dependence on irradiation dose, confocal spectral mapping of produced defects with varying irradiation dose, wide-field image of the irradiated flake in air and in liquid, bleaching of the emission of a FIB defect under continuous illumination, absorption spectra of defects before and after water treatment, AFM analysis of FIB-irradiated hBN flakes, AFM time lapse of the same irradiated hBN flake immersed in water, dependence of hole size on irradiation dose (dwell time), AFM analysis of suspended FIB-irradiated hBN flakes, artifacts of SMLM analysis of defect sites, processed wide-field images of fluorescent defects, effect of multiemitter fitting in ThunderSTORM on reconstruction of defects (PDF)

AUTHOR INFORMATION

Corresponding Authors

Evgenii Glushkov – *Laboratory of Nanoscale Biology, Institute of Bioengineering, Ecole Polytechnique Federale de Lausanne (EPFL), CH-1015 Lausanne, Switzerland;* orcid.org/0000-0001-7715-4524; Email: evgenii.glushkov@epfl.ch

Aleksandra Radenovic – *Laboratory of Nanoscale Biology, Institute of Bioengineering, Ecole Polytechnique Federale de Lausanne (EPFL), CH-1015 Lausanne, Switzerland;* orcid.org/0000-0001-8194-2785; Email: aleksandra.radenovic@epfl.ch

Authors

Michal Macha – *Laboratory of Nanoscale Biology, Institute of Bioengineering, Ecole Polytechnique Federale de Lausanne (EPFL), CH-1015 Lausanne, Switzerland*

Esther Räth – *Laboratory of Nano-Bio Instrumentation, Institute of Bioengineering, EPFL, CH-1015 Lausanne, Switzerland*

Vytautas Navikas – *Laboratory of Nanoscale Biology, Institute of Bioengineering, Ecole Polytechnique Federale de Lausanne (EPFL), CH-1015 Lausanne, Switzerland*

Nathan Ronceray – *Laboratory of Nanoscale Biology, Institute of Bioengineering, Ecole Polytechnique Federale de Lausanne (EPFL), CH-1015 Lausanne, Switzerland*

Cheol Yeon Cheon – *Laboratory of Nanoscale Electronics and Structures, Electrical Engineering Institute and Institute of Materials Science, EPFL, CH-1015 Lausanne, Switzerland*

Aqeel Ahmed – *Laboratory of Quantum Nano-Optics, Institute of Physics, EPFL, CH-1015 Lausanne, Switzerland*

Ahmet Avsar – *Laboratory of Nanoscale Electronics and Structures, Electrical Engineering Institute and Institute of Materials Science, EPFL, CH-1015 Lausanne, Switzerland; School of Mathematics, Statistics and Physics, Newcastle University, Newcastle upon Tyne NE1 7RU, United Kingdom*

Kenji Watanabe – *National Institute for Materials Science, 305-0044 Tsukuba, Japan;* orcid.org/0000-0003-3701-8119

Takashi Taniguchi – *National Institute for Materials Science, 305-0044 Tsukuba, Japan;* orcid.org/0000-0002-1467-3105

Ivan Shorubalko – *Laboratory for Transport at Nanoscale Interfaces, Empa–Swiss Federal Laboratories for Materials Science and Technology, 8600 Dübendorf, Switzerland;* orcid.org/0000-0001-9868-7303

Andras Kis – *Laboratory of Nanoscale Electronics and Structures, Electrical Engineering Institute and Institute of Materials Science, EPFL, CH-1015 Lausanne, Switzerland;* orcid.org/0000-0002-3426-7702

Georg Fantner – *Laboratory of Nano-Bio Instrumentation, Institute of Bioengineering, EPFL, CH-1015 Lausanne, Switzerland;* orcid.org/0000-0001-5889-3022

Complete contact information is available at: https://pubs.acs.org/10.1021/acsnano.1c07086

Author Contributions

[#]E.G. and M.M. contributed equally to this work.

Notes

The authors declare no competing financial interest.

The data that support the findings of this study are available from the corresponding authors on reasonable request.

The preprint version of this work is available online: Evgenii Glushkov, Michal Macha, Esther Rath, Vytautas Navikas, Nathan Ronceray, Cheol Yeon Cheon, Ahmet Avsar, Ahmed Aqeel, Kenji Watanabe, Takashi Taniguchi, Ivan Shorubalko, Andras Kis, Georg Fantner, and Aleksandra Radenovic. Engineering optically active defects in hexagonal boron nitride using focused ion beam and water, 2021, arXiv:2107.02254, https://arxiv.org/abs/2107.02254.

ACKNOWLEDGMENTS

The authors would like to acknowledge support from the EPFL Interdisciplinary Center for Electron Microscopy (CIME) and especially Lucy Navratilova for the help with

lamella preparation. E.G., V.N., and A.R. acknowledge the Max-Planck EPFL Center for Molecular Nanoscience and Technology as well as the NCCR Bioinspired Materials. M.M. acknowledges financial support from Swiss National Science Foundation (SNSF) Grant Number 200021$_1$92037. K.W. and T.T. acknowledge support from the Elemental Strategy Initiative conducted by MEXT, Japan, and CREST (JPMJCR15F3), JST.

REFERENCES

(1) Novoselov, K. S.; Mishchenko, A.; Carvalho, A.; Castro Neto, A. H. 2D materials andvan der Waals heterostructures. *Science* **2016**, *353*, 353.
(2) Atatüre, M.; Englund, D.; Vamivakas, N.; Lee, S.-Y.; Wrachtrup, J. Material platformsfor spin-based photonic quantum technologies. *Nat. Rev. Mater.* **2018**, *3*, 38−51.
(3) Radha, B.; Esfandiar, A.; Wang, F. C.; Rooney, A. P.; Gopinadhan, K.; Keerthi, A.; Mishchenko, A.; Janardanan, A.; Blake, P.; Fumagalli, L.; Lozada-Hidalgo, M.; Garaj, S.; Haigh, S. J.; Grigorieva, I. V.; Wu, H. A.; Geim, A. K. Molecular transport through capillaries made with atomic-scale precision. *Nature* **2016**, *538*, 222−225.
(4) Esfandiar, A.; Radha, B.; Wang, F. C.; Yang, Q.; Hu, S.; Garaj, S.; Nair, R. R.; Geim, A. K.; Gopinadhan, K. Size effect in ion transport through angstrom-scale slits. *Science* **2017**, *358*, 511−513.
(5) Fumagalli, L.; Esfandiar, A.; Fabregas, R.; Hu, S.; Ares, P.; Janardanan, A.; Yang, Q.; Radha, B.; Taniguchi, T.; Watanabe, K.; Gomila, G.; Novoselov, K. S.; Geim, A. K. Anomalously low dielectric constant of confined water. *Science* **2018**, *360*, 1339−1342.
(6) Caldwell, J. D.; Aharonovich, I.; Cassabois, G.; Edgar, J. H.; Gil, B.; Basov, D. N.Photonics with hexagonal boron nitride. *Nat. Rev. Mater.* **2019**, *4*, 552−567.
(7) Tran, T. T.; Bray, K.; Ford, M. J.; Toth, M.; Aharonovich, I. Quantum emission from hexagonal boron nitride monolayers. *Nat. Nanotechnol.* **2016**, *11*, 37−41.
(8) Kim, S.; Duong, N. M. H.; Nguyen, M.; Lu, T.-J.; Kianinia, M.; Mendelson, N.; Solntsev, A.; Bradac, C.; Englund, D. R.; Aharonovich, I. Integrated on Chip Platform with Quantum Emitters in Layered Materials. *Adv. Opt. Mater.* **2019**, *7*, 1901132.
(9) Kianinia, M.; Bradac, C.; Sontheimer, B.; Wang, F.; Tran, T. T.; Nguyen, M.; Kim, S.; Xu, Z.-Q.; Jin, D.; Schell, A. W.; Lobo, C. J.; Aharonovich, I.; Toth, M. All-optical control and super-resolution imaging of quantum emitters in layered materials. *Nat. Commun.* **2018**, *9*, DOI: 10.1038/s41467-018-03290-0.
(10) Feng, J.; Deschout, H.; Caneva, S.; Hofmann, S.; Lončarić, I.; Lazić, P.; Radenovic, A. Imaging of Optically Active Defects with Nanometer Resolution. *Nano Lett.* **2018**, *18*, 1739−1744.
(11) Comtet, J.; Glushkov, E.; Navikas, V.; Feng, J.; Babenko, V.; Hofmann, S.; Watanabe, K.; Taniguchi, T.; Radenovic, A. Wide-Field Spectral Super-Resolution Mapping of Optically Active Defects in Hexagonal Boron Nitride. *Nano Lett.* **2019**, *19*, 2516−2523.
(12) Glushkov, E.; Archetti, A.; Stroganov, A.; Comtet, J.; Thakur, M.; Navikas, V.; Lihter, M.; Marin, J. F. G.; Babenko, V.; Hofmann, S.; Manley, S.; Radenovic, A. Waveguide-Based Platform for Large-FOV Imaging of Optically Active Defects in 2D Materials. *ACS Photonics* **2019**, *6*, 3100−3107.
(13) Malein, R. N. E.; Khatri, P.; Ramsay, A. J.; Luxmoore, I. J. Stimulated Emission Depletion Spectroscopy of Color Centers in Hexagonal Boron Nitride. *ACS Photonics* **2021**, *8*, 1007−1012.
(14) Khatri, P.; Edward Malein, R. N.; Ramsay, A. J.; Luxmoore, I. J. Stimulated Emission Depletion Microscopy with Color Centers in Hexagonal Boron Nitride. *ACS Photonics* **2021**, *8*, 2081−2087.
(15) Comtet, J.; Grosjean, B.; Glushkov, E.; Avsar, A.; Watanabe, K.; Taniguchi, T.; Vuilleumier, R.; Bocquet, M.-L.; Radenovic, A. Direct observation of water-mediated single proton transport between hBN surface defects. *Nat. Nanotechnol.* **2020**, *15*, 598−604.
(16) Comtet, J.; Rayabharam, A.; Glushkov, E.; Zhang, M.; Avsar, A.; Watanabe, K.; Taniguchi, T.; Aluru, N. R.; Radenovic, A. Anomalous interfacial dynamics of single proton charges in binary aqueous solutions. *Sci. Adv.* **2021**, *7*, eabg8568.
(17) Chejanovsky, N.; Mukherjee, A.; Geng, J.; Chen, Y.-C.; Kim, Y.; Denisenko, A.; Finkler, A.; Taniguchi, T.; Watanabe, K.; Dasari, D. B. R.; Auburger, P.; Gali, A.; Smet, J. H.; Wrachtrup, J. Single-spin resonance in a van der Waals embedded paramagnetic defect. *Nat. Mater.* **2021**, *20*, 1079−1084.
(18) Gottscholl, A.; Kianinia, M.; Soltamov, V.; Orlinskii, S.; Mamin, G.; Bradac, C.; Kasper, C.; Krambrock, K.; Sperlich, A.; Toth, M.; Aharonovich, I.; Dyakonov, V. Initialization and read-out of intrinsic spin defects in a van der Waals crystal at room temperature. *Nat. Mater.* **2020**, *19*, 540−545.
(19) Kianinia, M.; White, S.; Fröch, J. E.; Bradac, C.; Aharonovich, I. Generation of Spin Defects in Hexagonal Boron Nitride. *ACS Photonics* **2020**, *7*, 2147−2152.
(20) Stern, H. L.; Gu, Q.; Jarman, J.; Eizagirre Barker, S.; Mendelson, N.; Chugh, D.; Schott, S.; Tan, H. H.; Sirringhaus, H.; Aharonovich, I.; Atatüre, M. Room-temperature optically detected magnetic resonance of single defects in hexagonal boron nitride. *Nat. Commun.* **2022**, *13*, 618.
(21) Gottscholl, A.; Diez, M.; Soltamov, V.; Kasper, C.; Sperlich, A.; Kianinia, M.; Bradac, C.; Aharonovich, I.; Dyakonov, V. Room temperature coherent control of spin defects in hexagonal boron nitride. *Sci. Adv.* **2021**, *7*, DOI: 10.1126/sciadv.abf3630.
(22) Caneva, S.; Weatherup, R. S.; Bayer, B. C.; Brennan, B.; Spencer, S. J.; Mingard, K.; Cabrero-Vilatela, A.; Baehtz, C.; Pollard, A. J.; Hofmann, S. Nucleation Control for Large, Single Crystalline Domains of Monolayer Hexagonal Boron Nitride via Si-Doped Fe Catalysts. *Nano Lett.* **2015**, *15*, 1867−1875.
(23) Koperski, M.; Vaclavkova, D.; Watanabe, K.; Taniguchi, T.; Novoselov, K. S.; Potemski, M. Midgap radiative centers in carbon-enriched hexagonal boron nitride. *Proc. Natl. Acad. Sci. U. S. A.* **2020**, *117*, 13214−13219.
(24) Choi, S.; Tran, T. T.; Elbadawi, C.; Lobo, C.; Wang, X.; Juodkazis, S.; Seniutinas, G.; Toth, M.; Aharonovich, I. Engineering and Localization of Quantum Emitters in Large Hexagonal Boron Nitride Layers. *ACS Appl. Mater. Interfaces* **2016**, *8*, 29642−29648.
(25) Yim, D.; Yu, M.; Noh, G.; Lee, J.; Seo, H. Polarization and Localization of Single-Photon Emitters in Hexagonal Boron Nitride Wrinkles. *ACS Appl. Mater. Interfaces* **2020**, *12*, 36362−36369.
(26) Vogl, T.; Campbell, G.; Buchler, B. C.; Lu, Y.; Lam, P. K. Fabrication and DeterministicTransfer of High-Quality Quantum Emitters in Hexagonal Boron Nitride. *ACS Photonics* **2018**, *5*, 2305−2312.
(27) Fischer, M.; Caridad, J. M.; Sajid, A.; Ghaderzadeh, S.; Ghorbani-Asl, M.; Gammelgaard, L.; Bøggild, P.; Thygesen, K. S.; Krasheninnikov, A. V.; Xiao, S.; Wubs, M.; Stenger, N. Controlled generation of luminescent centers in hexagonal boron nitride by irradiation engineering. *Sci. Adv.* **2021**, *7*, eabe7138.
(28) Toledo, J. R.; de Jesus, D. B.; Kianinia, M.; Leal, A. S.; Fantini, C.; Cury, L. A.; Sáfar, G.A. M.; Aharonovich, I.; Krambrock, K. Electron paramagnetic resonance signature of point defects in neutron-irradiated hexagonal boron nitride. *Phys. Rev. B* **2018**, *98*, 1−6.
(29) Hayee, F.; Yu, L.; Zhang, J. L.; Ciccarino, C. J.; Nguyen, M.; Marshall, A. F.; Aharonovich, I.; Vučković, J.; Narang, P.; Heinz, T. F.; Dionne, J. A. Revealing multiple classes of stable quantum emitters in hexagonal boron nitride with correlated optical and electron microscopy. *Nat. Mater.* **2020**, *19*, 534−539.
(30) Proscia, N. V.; Shotan, Z.; Jayakumar, H.; Reddy, P.; Cohen, C.; Dollar, M.; Alkauskas, A.; Doherty, M.; Meriles, C. A.; Menon, V. M. Near-deterministic activation of room-temperature quantum emitters in hexagonal boron nitride. *Optica* **2018**, *5*, 1128.
(31) Li, C.; Mendelson, N.; Ritika, R.; Chen, Y.; Xu, Z.-Q.; Toth, M.; Aharonovich, I. Scalable and Deterministic Fabrication of Quantum Emitter Arrays from Hexagonal Boron Nitride. *Nano Lett.* **2021**, *21*, 3626−3632.
(32) Hou, S.; Birowosuto, M. D.; Umar, S.; Anicet, M. A.; Tay, R. Y.; Coquet, P.; Tay, B. K.; Wang, H.; Teo, E. H. T. Localized emission

from laser-irradiated defects in 2D hexagonal boron nitride. *2D Mater.* **2018**, *5*, 015010.
(33) Gao, X.; Pandey, S.; Kianinia, M.; Ahn, J.; Ju, P.; Aharonovich, I.; Shivaram, N.; Li, T. Femtosecond Laser Writing of Spin Defects in Hexagonal Boron Nitride. *ACS Photonics* **2021**, *8*, 994−1000.
(34) Fournier, C.; Plaud, A.; Roux, S.; Pierret, A.; Rosticher, M.; Watanabe, K.; Taniguchi, T.; Buil, S.; Quélin, X.; Barjon, J.; Hermier, J.-P.; Delteil, A. Position controlled quantum emitters with reproducible emission wavelength in hexagonal boron nitride. *Nat. Commun.* **2021**, *12*, DOI: 10.1038/s41467-021-24019-6.
(35) Ziegler, J.; Klaiss, R.; Blaikie, A.; Miller, D.; Horowitz, V. R.; Alemán, B. J. Deterministic Quantum Emitter Formation in Hexagonal Boron Nitride via Controlled Edge Creation. *Nano Lett.* **2019**, *19*, 2121−2127.
(36) Fox, D. S.; Zhou, Y.; Maguire, P.; O'Neill, A.; Ó'Coileáin, C.; Gatensby, R.; Glushenkov, A. M.; Tao, T.; Duesberg, G. S.; Shvets, I. V.; Abid, M.; Abid, M.; Wu, H.- C.; Chen, Y.; Coleman, J. N.; Donegan, J. F.; Zhang, H. Nanopatterning and Electrical Tuning of MoS2 Layers with a Subnanometer Helium Ion Beam. *Nano Lett.* **2015**, *15*, 5307−5313.
(37) Mupparapu, R.; Steinert, M.; George, A.; Tang, Z.; Turchanin, A.; Pertsch, T.; Staude, I. Facile Resist-Free Nanopatterning of Monolayers of MoS2 by Focused Ion-Beam Milling. *Adv. Mater. Interfaces* **2020**, *7*, 2000858.
(38) Giannuzzi, L.; Smith, N. TEM Specimen Preparation with Plasma FIB Xe+ Ions. *Microsc. Microanal.* **2011**, *17*, 646−647.
(39) Zhong, X.; Wade, C. A.; Withers, P. J.; Zhou, X.; Cai, C.; Haigh, S. J.; Burke, M. G. Comparing Xe + pFIB and Ga + FIB for TEM sample preparation of Al alloys: Minimising FIB-induced artefacts. *J. Microsc* **2021**, *282*, 101−112.
(40) Schué, L.; Stenger, I.; Fossard, F.; Loiseau, A.; Barjon, J. Characterization methods dedicated to nanometer-thick hBN layers. *2D Mater.* **2017**, *4*, 015028.
(41) Taniguchi, T.; Watanabe, K. Synthesis of high-purity boron nitride single crystals under high pressure by using Ba−BN solvent. *J. Cryst. Growth* **2007**, *303*, 525−529.
(42) Ovesný, M.; Křížek, P.; Borkovec, J.; Švindrych, Z.; Hagen, G. M. ThunderSTORM: A comprehensive ImageJ plug-in for PALM and STORM data analysis and super-resolution imaging. *Method. Biochem. Anal.* **2014**, *30*, 2389−2390.
(43) Turiansky, M. E.; Alkauskas, A.; Bassett, L. C.; Van de Walle, C. G. Dangling Bonds in Hexagonal Boron Nitride as Single-Photon Emitters. *Phys. Rev. Lett.* **2019**, *123*, DOI: 10.1103/PhysRevLett.123.127401.
(44) Streletskii, A. N.; Permenov, D. G.; Bokhonov, B. B.; Leonov, A. V.; Mudretsova, S. N. Mechanochemistry of hexagonal boron nitride. 2. Reactivity upon interaction with water. *Colloid J.* **2010**, *72*, 553−558.
(45) Speiser, A.; Müller, L.-R.; Hoess, P.; Matti, U.; Obara, C. J.; Legant, W. R.; Kreshuk, A.; Macke, J. H.; Ries, J.; Turaga, S. C. Deep learning enables fast and dense single-molecule localization with high accuracy. *Nat. Methods* **2021**, *18*, 1082−1090.
(46) Kalhor, N.; Boden, S. A.; Mizuta, H. Sub-10nm patterning by focused He-ion beammilling for fabrication of downscaled graphene nano devices. *Microelectron. Eng.* **2014**, *114*, 70−77.
(47) Buchheim, J.; Wyss, R. M.; Shorubalko, I.; Park, H. G. Understanding the interaction between energetic ions and freestanding graphene towards practical 2D perforation. *Nanoscale* **2016**, *8*, 8345−8354.
(48) Shorubalko, I.; Choi, K.; Stiefel, M.; Park, H. G. Ion beam profiling from the interaction with a freestanding 2D layer. *Beilstein J. Nanotechnol.* **2017**, *8*, 682−687.
(49) Bradac, C.; Xu, Z.-Q.; Aharonovich, I. Quantum Energy and Charge Transfer at Two- Dimensional Interfaces. *Nano Lett.* **2021**, *21*, 1193−1204.
(50) Odermatt, P. D.; Shivanandan, A.; Deschout, H.; Jankele, R.; Nievergelt, A. P.; Feletti, L.; Davidson, M. W.; Radenovic, A.; Fantner, G. E. High-Resolution Correlative Microscopy: Bridging the Gap between Single Molecule Localization Microscopy and Atomic Force Microscopy. *Nano Lett.* **2015**, *15*, 4896−4904.
(51) Geissbuehler, S.; Bocchio, N. L.; Dellagiacoma, C.; Berclaz, C.; Leutenegger, M.; Lasser, T. Mapping molecular statistics with balanced super-resolution optical fluctuation imaging (bSOFI). *Opt. Nanosc.* **2012**, *1*, 4.